INORGANIC CHEMISTRY
FRONTIERS

RESEARCH ARTICLE

View Article Online
View Journal | View Issue

Check for updates

Cite this: *Inorg. Chem. Front.*, 2023, **10**, 1614

Solvent-controlled synthesis of an Al_{12}-oxo molecular ring and Al_{24}-oxo truncated metallo-cube†

Ying Zou, Wei Lv, Zhen-Zhen Xue, Jin-Hua Li, Xiao-Yu Li * and Guo-Ming Wang *

Received 21st November 2022,
Accepted 27th January 2023

DOI: 10.1039/d2qi02461f

rsc.li/frontiers-inorganic

Highly symmetrical molecules with beautiful geometries are ubiquitous in nature. It has inspired creative ideas of the perfect combination of geometry and molecular structural chemistry. Some metal clusters with regular geometric polyhedra have been reported, but such highly symmetric polyhedra for Al-oxo clusters are really scarce on account of the fast hydrolysis of Al^{3+} ions. Herein, a $[Al_{12}(CH_3O)_{24}(NAP)_{12}]\cdot 4DMF\cdot 2H_2O\cdot 2CH_3OH$ (**Al_{12}**, NAP^- = 2-naphthoic acid) nanoring was synthesized by the solvothermal reaction of $AlCl_3\cdot 6H_2O$, 2-naphthoformic acid (HNAP) and triethylamine (Et_3N) in CH_3OH and DMF. Interestingly, the regulation from ring-shaped **Al_{12}** to $[Al_{24}(OH)_{32}(CH_3O)_{22}(CH_3OH)_2(NAP)_{12}]\cdot 6Cl\cdot 2H_2O\cdot 2CH_3OH$ (**Al_{24}**) metallocage is realized by only changing the reactive solvents. The **Al_{24}** metallocage can be seen as one of 13 Archimedean polyhedra, a truncated cube composed of eight Al_3 triangles and six Al_8 octagons by sharing vertical Al^{3+} ions. In addition, high-resolution electrospray ionization mass spectrometry (HR-ESI-MS) reveals that the metallic skeletons of **Al_{12}** and **Al_{24}** can be maintained stable in CH_3OH and CH_2Cl_2. Furthermore, **Al_{12}** and **Al_{24}** emit blue luminescence and exhibit photocurrent responses under LED light illumination.

Published on 28 1 2023. Downloaded on 2025/10/16 18:37:51.

Introduction

Highly symmetrical polyhedra have intrigued various professional researchers in the fields of mathematics, biology, aesthetics, architecture, and chemistry for thousands of years.[1–6] The classical polyhedra contain 5 platonic polyhedra constructed by one kind of regular convex polygon with the same number of faces at each vertex, and 13 Archimedean polyhedra composed of two or more types of regular polygons.[7] In chemistry, these exemplifications have been found in coordination molecular nanocages and nanoclusters of coordination chemistry.[8] For coordination nanocages, based on the construction rules of polyhedra, suitable organic ligands with specific configurations are often selected for their syntheses.[9–14] However, the nanoclusters assembled from simple ingredients are elusory and the acquisition of geometric structures lacks the presupposition. As a famous polyhedral cluster, C_{60} is constructed by 12 pentagons and 20 hexagons, which is a classical Archimedean polyhedron, truncated icosahedron, inspiring various creative ideas for building fullerene-like nanopolyhedral metal clusters.[15] After long-term unremitting efforts, transition/lanthanide metal clusters with Platonic and Archimedean polyhedra have been isolated, such as V_{24},[16] Co_{32},[17] Cd_{66},[18] Mo_{240},[19] Pd_{145},[20] Ag_{180},[21] and Ln_{104}.[22]

As the most abundant metal element in the earth's crust, Al clusters with lightweight and high stability have potential applications in environmental science, geochemistry, biology, optical, and adsorption materials.[23,24] Aqueous aluminum chemistry presents a series of typical aluminum oxo-hydroxo polycation aggregations, as exemplified by flat-Al_{13} $[Al_{13}(OH)_{24}(H_2O)_{24}]^{15+}$,[25,26] isomers of the Al_{13}-Keggin cluster $[Al_{13}O_4(OH)_{24}(H_2O)_{12}]^{7+}$,[24,27] and larger Al_{30} clusters $[Al_{30}O_8(OH)_{56}(H_2O)_{26}]^{18+}$.[24,28] They were produced from hydrolytic processes of Al^{3+} ions in aqueous solutions, which is actually intricate and affected by olation reactions, formation of precursors, aggregation, nucleation and crystallization.[24,27] An effective route is to choose suitable trapping ligands, such as Al_3 and Al_8 protected by the trisilanol ligand,[29] a supramolecular zeotype Al_{15} constructed using hpdta (H_5hpdta = $HOCH_2[CH_2N(CH_2COOH)_2]_2$).[30] Although many efforts have been made to investigate the aqueous aluminum chemistry of hydrolysis and polymerization of Al^{3+} ions, the relationship of solution equilibria and the existence of polynuclear species is still complex and unpredictable.[31] For this dilemma, recently, a new strategy known as coordination delayed hydrolysis has been adopted by Zhang *et al.* to synthesize a series of Al-oxo clusters by choosing monodentate carboxylic acid ligands and organic aluminium salts under solvothermal conditions.[32–35]

College of Chemistry and Chemical Engineering, Qingdao University, Shandong 266071, China. E-mail: xylichem@qdu.edu.cn, gmwang_pub@163.com

†Electronic supplementary information (ESI) available. CCDC 2163632 and 2163633. For ESI and crystallographic data in CIF or other electronic format see DOI: https://doi.org/10.1039/d2qi02461f

This journal is © the Partner Organisations 2023

Published on 28 1 2023. Downloaded on 2025/10/16 18:37:51.

Most of these Al-oxo clusters feature the structures of molecular rings from Al_8 to the largest Al_{20} constructed using different large conjugated carboxylic acids.[33,34,36] The different peripheral ligands realize luminescence modulation of Al_{20} molecular rings from blue to green. Besides, other Al clusters also display luminescence properties, which originated from the luminescence of the corresponding ligands.[37] Nevertheless, highly symmetric aluminum-oxo clusters are rare because of the rapid hydrolysis of Al^{3+} ions and the difficult precipitation of high-quality and determinable single crystals.[36] Many efforts will be made to further explore the assembly and luminescence properties of aluminum-oxo clusters.

Based on these considerations, enlightened by the simple one-pot solvothermal synthesis method of transition/lanthanide metal clusters accompanied by adding alkali to control the hydrolysis of metal ions, a ring **Al_{12}** dodecagon with the formula, $[Al_{12}(CH_3O)_{24}(NAP)_{12}]\cdot 4DMF\cdot 2H_2O\cdot 2CH_3OH$ was obtained in CH_3OH–DMF by the reaction of monodentate carboxylic acid and inorganic aluminium salt with Et_3N to adjust the alkalinity of the solution. When using CH_3OH–CH_3CN as the solvent, a new Archimedean polyhedron **Al_{24}**, $[Al_{24}(OH)_{32}(CH_3O)_{22}(CH_3OH)_2(NAP)_{12}]\cdot 6Cl\cdot 2H_2O\cdot 2CH_3OH$ was isolated. It features a truncated-cube metallocage containing 8 Al_3 triangles and 6 Al_8 octagons. This work successfully realizes the regulation of Al-oxo skeletons from molecular ring to metallocage. Moreover, the metallic cores of **Al_{12}** and **Al_{24}** have good stability in methanol and dichloromethane with the ligand exchange. Furthermore, the photocurrent response and the temperature-responsive luminescence behaviour of the **Al_{12}** and **Al_{24}** were investigated.

Experimental

Materials and physical measurements

Chemicals and solvents were purchased without further purification. On an ABB Bomen MB 102 series FT-IR (KBr pellets) spectrometer, IR spectra were recorded in the 4000–400 cm^{-1} region. The elemental analyses were conducted on a Vario EL cube analyzer. Powder X-ray diffraction (PXRD) data were obtained on the Rigaku SmartLab X-ray diffractometer. Thermogravimetric (TG) curves were measured from ambient temperature to 800 °C using the SDT Q600 analyzer. A Puxi Tu-1901 spectrophotometer was used to measure UV-vis spectra. A Bruker Impact II high-definition mass spectrometer quadrupole and time-of-flight (Q/TOF) modules were used to record the mass spectra (HR-ESI-MS). The photocurrent experiments were performed on a CHI660E electrochemistry workstation. The 10 L of naphthol (0.5 wt%) and 5 mg samples of **Al_{12}** or **Al_{24}** were combined with 0.5 mL of ethanol and then subjected to a 30-minute sonication process. The coated film was produced by pipetting 150 μL solution onto the cleaned ITO glass after evaporation. A Pt wire served as the counter electrode, an Ag/AgCl electrode served as the reference electrode, and the produced ITO glass film served as the working electrode. The medium was an aqueous solution of Na_2SO_4 (0.2 M). An F-4700 fluorescence spectrometer was used to measure the room-temperature fluorescence. The Edinburgh spectrofluorometer (FLS980), with a cryostat to regulate temperature, was used to collect variable-temperature fluorescence data. After a 10-minute homeothermy, each data was collected and quantum yield data were obtained on the integrating sphere, and the luminescence lifetimes were determined on the same device using a time-correlated single-photon counting method (FLS980).

Synthesis of Al_{24}

A mixture of 2-naphthoformic acid (HNAP, 172.2 mg, 1 mmol), $AlCl_3\cdot 6H_2O$ (500 mg, 2 mmol), were dissolved in a mixed solvent of CH_3OH (3 mL) : CH_3CN (8 mL) in a 23 mL Teflon-lined reaction vessel, then 0.5 mL triethylamine (Et_3N) were added into the mixture under stirring, finally kept at 100 °C for 4 days. When slowly cooled to room temperature, washed with CH_3OH, and dried in the air, colorless block crystals were obtained (yield 35.62% based on $AlCl_3\cdot 6H_2O$). Elemental analyses calcd. (found) for **Al_{24}**: $C_{158}H_{202}Al_{24}Cl_6O_{84}$: C, 44.08 (43.89); H, 4.73 (4.92)%. Selected IR peaks (cm^{-1}): 3450 (s), 3060 (w), 2950 (m), 2840 (w), 2670 (w),1610 (s), 1570 (m), 1480 (s), 1430 (s), 1070 (m), 982 (m), 870 (m), 796 (s), 594 (s), 501 (w).

Synthesis of Al_{12}

The **Al_{12}** is similar to **Al_{24}** except for CH_3OH : CH_3CN (11 mL, v : v = 3 : 8) was replaced by CH_3OH and DMF (10 mL, v : v = 1 : 1), colorless lamellar crystals were obtained (yield 40.56% based on $AlCl_3\cdot 6H_2O$). Elemental analyses calcd. (found) for **Al_{12}**: $C_{170}H_{196}Al_{12}N_4O_{56}$: C, 58.09 (57.87); H, 5.62 (5.78); N, 1.59 (1.62)%. Selected IR peaks (cm^{-1}): 3434 (s), 2964 (m), 2925 (m), 2856 (m), 2296 (w), 1629 (s), 1381 (m), 1080 (m), 1043 (m), 929 (w), 879 (w), 565 (w).

X-ray crystallography

Single crystals of **Al_{24}** and **Al_{12}** with the appropriate dimensions were selected under an optical microscope, coated fast into high vacuum grease, and put on a glass fiber for single-crystal data collection with Cu Kα radiation on the Rigaku XtaLAB MM007 CCD diffractometer. OLEX[38] and SHELXL-97 were used to directly solve the structures.[39] Based on the relevant atoms and refined with predetermined temperature factors, all hydrogen atoms were theoretically hydrogenated. To ensure that no extra symmetry could be given to the models, the Addsym function of PLATON[40] was used to check each structure. The SQUEEZE command was used to eliminate the disorganized solvent molecules. The Cambridge Crystallographic Data Centre (CCDC) has received the crystallographic information from this article (CCDC: 2163632 (**Al_{12}**); 2163633 (**Al_{24}**)).† Table S6† provides the pertinent crystallographic data. Table S7† displays the selected bond lengths and angles.

Published on 28 1 2023. Downloaded on 2025/10/16 18:37:51.

Results and discussion

Crystal structure of Al_{12} cluster

Single-crystal X-ray diffraction analysis revealed that the **Al_{12}** cluster crystallizes in the triclinic $P\bar{1}$ space group and it contains 12 Al^{3+}, 12 NAP^-, and 24 CH_3O^- (Fig. 1a). Twelve Al^{3+} ions form a complanate dodecagon with the Al–Al distances in the range of 2.8621–2.8781 Å and every Al^{3+} ion is located on the vertex of a dodecagon. The diameter of the **Al_{12}** metal ring is about 9.93 Å. The whole **Al_{12}** cluster is stabilized by 12 NAP^- and 24 CH_3O^-, which can be divided into three layers (Fig. 1b). The peripheral ligands of the middle layer contain six NAP^- ligands and six CH_3O^-, which alternately array to form a large outer ring parallel to the **Al_{12}** metal dodecagon (Fig. 1c). The inner part of the middle layer is filled with parallel six CH_3O^-, in which three face up and three faces down. The upper and lower two ligand layers vertical to the **Al_{12}** metal dodecagon are identical and every layer comprises three NAP^- and six CH_3O^- (Fig. 1d). Every two methanol molecules are sandwiched between two NAP^- ligands. All Al^{3+} ions of **Al_{12}** cluster adopt six-coordinated distorted octahedral geometry with six O atoms from 2 NAP^- and 4 CH_3O^-. The NAP^- and CH_3O^- respectively adopt μ_2–η^1:η^1 and μ_2 connection modes. The Al–O distances and O–Al–O angles are in the range of 1.850–1.946 Å and 77.01–175.27°, respectively.

Crystal structure of Al_{24} cluster

Similar to the synthesis of **Al_{12}**, one new **Al_{24}** cluster with the formula $[Al_{24}(OH)_{32}(CH_3O)_{22}(CH_3OH)_2(NAP)_{12}]\cdot 6Cl\cdot 2H_2O\cdot 2CH_3OH$ was obtained by using the solvent of CH_3OH–CH_3CN. It crystallizes in the monoclinic $P21/n$ space group and the asymmetric unit contains half an **Al_{24}** cluster. As shown in Fig. 2a, the **Al_{24}** molecular skeleton is composed of eight $[Al_3(OH)(CH_3O)_3]$ in the truncated positions and six open $[Al_8(OH)_4(CH_3O)_4(NAP)_4]$ windows. The $[Al_3(OH)(CH_3O)_3]$ building block is coordinated by 3 CH_3O^- capped on the Al–Al sides and 1 OH^- stamped over the centre of the triangle (Fig. 2b). The $[Al_8(OH)_4(CH_3O)_4(NAP)_4]$ consists of four NAP^- and OH^-, both capped on the interval four sides, and the remaining four sides are fixed by four CH_3O^- (Fig. 2c). The **Al_{24}** is a cation cluster with six free Cl^- ions in the centre of octagonal windows bonded to the **Al_{24}** frame by hydrogen-bond interactions, which are formed with four μ_2-OH^- in the interior of the octagon with the Cl···O distances in the range of 3.174–3.302 Å and the Cl···H–O angles in the range of 161.16–165.06° (Table S4†). This Cl^- template interaction is frequently found in the lanthanide clusters, such as Dy_{76},[41] Ln_{48},[42–44] and Ln_{15}.[45–47] The **Al_{24}** metallic inner features a truncated cube (Fig. 2d) with a small 7 Å diameter, though the total molecular **Al_{24}** cluster with a larger 2.0 nm diameter due to the peripheral big NAP^- ligands. The Al–Al interactions are in the range of 2.853(3)–2.976(3) Å.

The Al clusters are also a kind of metallic hydroxide clusters. The simplified Al/O core of **Al_{24}** (Fig. 3c) is composed of the simplified trigonal $[Al_3(OH)O_3]$ and octagonal $[Al_8(OH)_8O_4]$ (Fig. 3a and b) by sharing the sides of the triangles. As depicted in Fig. 3f, the further simplified metal skeleton belongs to one of the 13 Archimedean polyhedra, a truncated cube comprising 8 Al_3 triangles on the truncated positions of the cube (Fig. 3d) and 6 Al_8 octagons on the six faces (Fig. 3e) with the strong Al–Al interactions in the range of 2.850–2.978 Å. This Archimedean polyhedron is rare in the metal nanoclusters, compared with the truncated tetrahedron

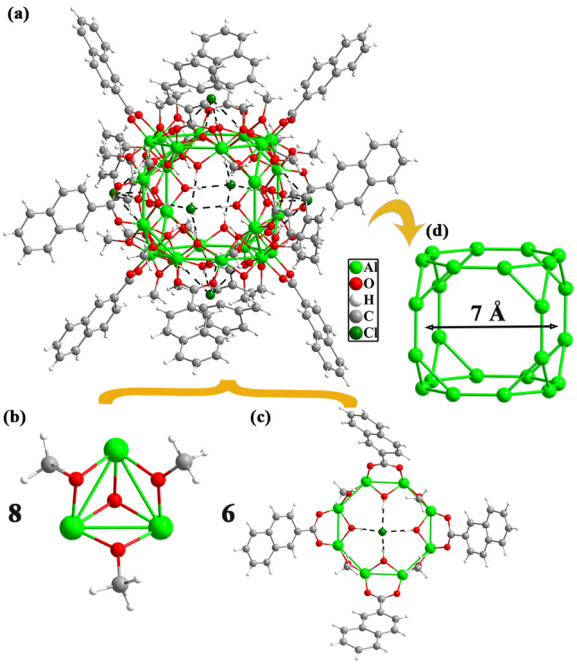

Fig. 2 (a) Molecular structures of **Al_{24}**. (b) and (c) The $[Al_3(OH)(CH_3O)_3]$ and $[Al_8(OH)_4(CH_3O)_4(NAP)_4]$ building blocks. (d) The 24-nuclearity Al metallic skeleton with a truncated hexahedral geometry (green: Al; red: O; grey: C; dark green: Cl; white: H).

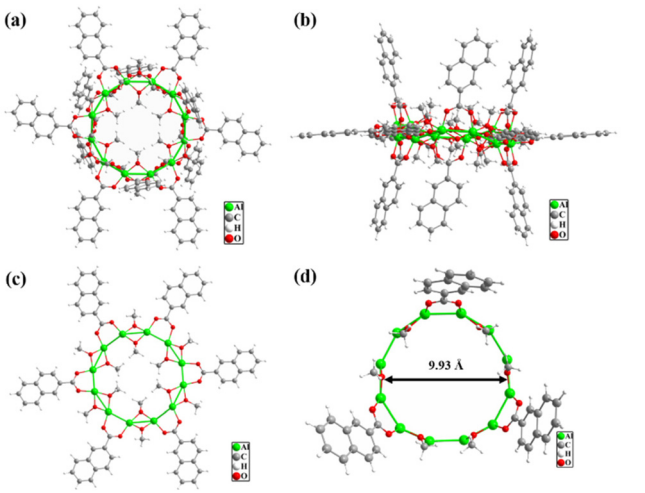

Fig. 1 (a) and (b) Molecular structures of **Al_{12}** at different view directions. (c) and (d) The ligand arrangement of the middle and upper/lower layers of **Al_{12}** (green: Al; red: O; grey: C; white: H).

This journal is © the Partner Organisations 2023

Published on 28 1 2023. Downloaded on 2025/10/16 18:37:51.

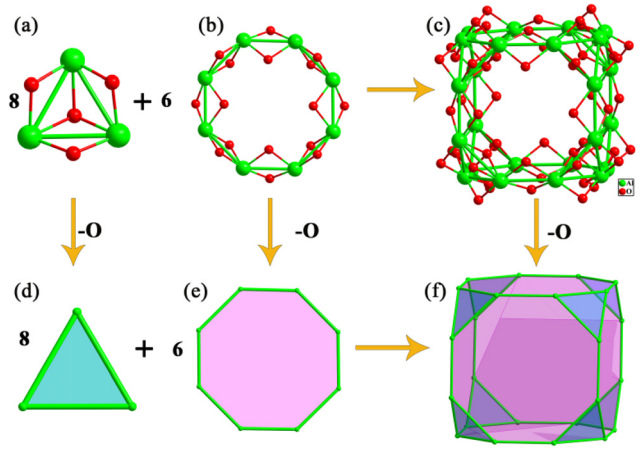

Fig. 3 (a) and (b) $[Al_3(OH)O_3]$ and $[Al_8(OH)_8O_4]$ building units. (c) The Al/O core of $\mathbf{Al_{24}}$. (d) and (e) The simplified Al_3 triangle (blue) and Al_8 octagon (purple). (f) The Archimedean polyhedron of $\mathbf{Al_{24}}$ metallic core (green: Al; red: O).

(Ag_{37}),[48] truncated octahedron (Co_{32}),[49] truncated icosahedron (Ln_{60}),[50] whereas some similar M_{24} coordination molecular cages with the organic ligands as the linkers have been reported.[51,52]

All Al^{3+} ions in the $\mathbf{Al_{24}}$ cluster adopt six-coordinated distorted octahedral geometry with six O atoms from 3 OH^-, 1 NAP^- and 2 CH_3O^-. The Al–O contacts and O–Al–O angles are in the range of 1.823–1.987 Å and 74.97–171.3°, respectively. All 12 NAP^- ligands are situated at the sides of the octagons by adopting a μ_2–η^1:η^1 connection mode (Fig. S1a†). The 32 OH^- can be divided into two types, namely, 24 μ_2-OH^- is uniformly oriented to the centre of 6 octagon (Fig. S1b†), which are at the opposite positions of every NAP^- ligand, whereas the residual 8 μ_3-OH^- are capped on the centre of the 8 trigonal Al_3 building blocks (Fig. S1c†). For the CH_3O^- ligands, all are located on the sharing Al–Al sides of triangular Al_3 and octagonal Al_8 building blocks (Fig. S1d†).

Chemical stability and TG analyses

The stability of $\mathbf{Al_{24}}$ and $\mathbf{Al_{12}}$ was measured by immersing their single crystals in water and typical organic solvents. According to the comparison of the experimental and simulated powder X-ray diffraction (PXRD) patterns (Fig. S9†), $\mathbf{Al_{24}}$ can be kept stable in CH_3OH, EtOH, CH_3CN, and H_2O at least for a day. For $\mathbf{Al_{12}}$, it displays very good stability in CH_3OH, EtOH, CH_3CN, H_2O, and DMF for a month (Fig. S10†). The above findings demonstrate that $\mathbf{Al_{24}}$ and $\mathbf{Al_{12}}$ exhibit high chemical stability in some solvents and H_2O. As shown in Fig. S8c and S8d,† the experimental IR spectra of $\mathbf{Al_{12}}$ and $\mathbf{Al_{24}}$ after immersing their single crystals in water and typical organic solvents were measured to further show their stabilities. Additionally, dry solid samples of $\mathbf{Al_{24}}$ and $\mathbf{Al_{12}}$ were used to study the thermal stability under the N_2 environment from 30 to 800 °C (Fig. S11†). Two H_2O and two CH_3OH molecules were removed from $\mathbf{Al_{24}}$ during a slight weight loss of 2.33% up to 210 °C (calcd 2.35%). The mass loss from 210 to 285 °C is due to the departure of 24 coordinated methanol molecules (exp 17.98%, calcd 17.34%). As the temperature increased to 615 °C, the naphthalene rings of the organic NAP^- ligands began to break down and the mass fraction of 39.50% was lost (calcd 39.00%). For $\mathbf{Al_{12}}$, the first weight loss below 185 °C was ascribed to the removal of four DMF, two H_2O, and two CH_3OH molecules (exp 11.16%, calcd 11.21%). Next, the weight loss of 47.86% from 260 to 440 °C is ascribed to the removal of the naphthalene rings from the NAP^- ligands (calcd 47.51%). The third weight loss from 500 to 615 °C corresponds to the decomposition of coordinated methanol molecules.

Solution behaviours of Al_{24} and Al_{12} clusters

The high-resolution electrospray ionization mass spectrometry (ESI-MS) can be used to determine the fragment composition and charge state of the metal clusters.[21,53–60] The negative-mode ESI-MS of $\mathbf{Al_{24}}$ was investigated by dissolving the crystals in CH_3OH–CH_2Cl_2 to analyse its solution stability. As shown in Fig. 4, there are two sets of peaks in the mass-to-charge (m/z) ratio ranges of 2000–2100 (1) with −2 charge and 4000–4200 (2) with −1 charge, respectively. For 1 group, the distances between two neighbouring peaks are disparate with 6.51, 7.51, 6.55, 7.47, 7.00, and 7.51 having no uniform variation trend for the seven species (**1a**–**1g**). Their compositions, at the positions: m/z = 2045.78, 2052.20, 2059.79, 2066.22, 2073.79, 2080.79, and 2088.20, can be identified by matching the experimental and simulated isotopic distributions with the corresponding formulas, $[Al_{24}(OH)_{34}(CH_3O)_{26}(NAP)_{11}(H_2O)_4Cl_3]^{2-}$, $[Al_{24}(OH)_{34}(CH_3O)_{23}(NAP)_{11}(H_2O)_4Cl_6]^{2-}$, $[Al_{24}(OH)_{32}(CH_3O)_{28}(NAP)_{11}(H_2O)_4Cl_3]^{2-}$, $[Al_{24}(OH)_{32}(CH_3O)_{25}(NAP)_{11}(H_2O)_4Cl_6]^{2-}$, $[Al_{24}(OH)_{31}(CH_3O)_{30}(NAP)_{11}(H_2O)_1Cl_4H_2]^{2-}$, $[Al_{24}(OH)_{31}(CH_3O)_{31}(NAP)_{11}Cl_4H_3]^{2-}$, $[Al_{24}(OH)_{34}(CH_3O)_{23}(NAP)_{11}(H_2O)_6Cl_7H_1]^{2-}$ (Table S1†). This set of signals indicates that the metal skeleton of $\mathbf{Al_{24}}$ cluster is stable in CH_3OH–CH_2Cl_2, whereas the protection groups of OH^-, CH_3O^-, and NAP^- exist in the coordination–

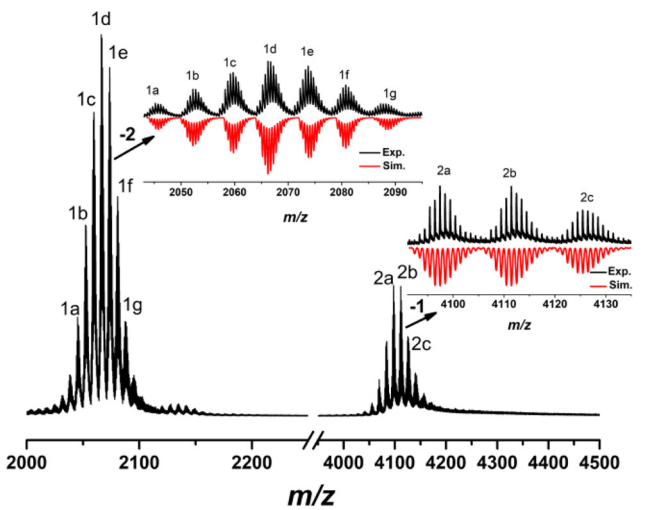

Fig. 4 The negative-ion ESI-MS of $\mathbf{Al_{24}}$ in CH_3OH/CH_2Cl_2. Inset: the experimental isotropic pattern (block) and simulated (red) data.

Published on 28 1 2023. Downloaded on 2025/10/16 18:37:51.

disassociation equilibrium. The most dominant peak (1d) with the composition of $[Al_{24}(OH)_{32}(CH_3O)_{25}(NAP)_{11}(H_2O)_4Cl_6]^{2-}$ at m/z = 2066.22 is approximate to the parent cluster except for one NAP^- replaced with one CH_3O^-. For the 2 groups, **2a–2c** has similar distances of 14.02 corresponding to $[+CH_3O^- - H_2O + H^+]$ with the formulas, $[Al_{22}(OH)_{23}(CH_3O)_{25}(NAP)_{12}(H_2O)_2Cl_7]^-$, $[Al_{22}(OH)_{23}(CH_3O)_{26}(NAP)_{12}(H_2O)_1Cl_7H_1]^-$, $[Al_{22}(OH)_{23}(CH_3O)_{27}(NAP)_{12}Cl_7H_2]^-$ at m/z = 4097.45, 4111.47 and 4125.48, suggesting the presence of the Al_{22} fragments in the CH_3OH–CH_2Cl_2 of **Al_{24}**.

The positive-ion ESI-MS data of **Al_{24}** was also monitored at m/z = 500–6000 (Fig. 5) by dissolving its crystals in CH_3OH–CH_2Cl_2. There are four groups (**1a–1f**, **2a–2g**, **3a–3g**, and **4a–4e**) of experimental peaks at m/z = 1950–2250 with +2 charge (see inset in Fig. S2†). By matching the experimental and simulated isotopic distributions, all formulas of fragments are listed in Table S2.† The formulas of **2c–2f** ($[Al_{24}(OH)_{32}(CH_3O)_{24}(NAP)_{12}Cl_2(H_2O)_x(CH_3OH)_{3-x}]^{2+}$, x = 3, 2, 1, 0), **3a–3f** ($[Al_{24}(OH)_{32}(CH_3O)_{24}(NAP)_{12}Cl_2(H_2O)_5(CH_3CN)_1(CH_3OH)_1]^{2+}$ (**3a**); $[Al_{24}(OH)_{32}(CH_3O)_{24}(NAP)_{12}Cl_2(H_2O)_3(CH_3CN)_3]^{2+}$ (**3b**); $[Al_{24}(OH)_{32}(CH_3O)_{24}(NAP)_{12}Cl_2(H_2O)_2(CH_3CN)_3(CH_3OH)_1]^{2+}$ (**3c**); $[Al_{24}(OH)_{32}(CH_3O)_{24}(NAP)_{12}Cl_3(H_2O)_4(CH_3OH)_3H_1]^{2+}$ (**3d**); $[Al_{24}(OH)_{32}(CH_3O)_{24}(NAP)_{12}Cl_4(H_2O)_1(CH_3OH)_4H_2]^{2+}$ (**3e**); $[Al_{24}(OH)_{32}(CH_3O)_{24}(NAP)_{12}Cl_4(CH_3OH)_5H_2]^{2+}$ (**3f**)) and **4a–4e** ($[Al_{24}(OH)_{32}(CH_3O)_{24}(NAP)_{12}Cl_2(H_2O)_x(CH_3CN)_4(CH_3OH)_{6-x}]^{2+}$, x = 3, 2, 1, 0) are consistent with the molecular formulas of **Al_{24}** ($[Al_{24}(OH)_{32}(CH_3O)_{22}(CH_3OH)_2(NAP)_{12}]\cdot 6Cl\cdot 2H_2O\cdot 2CH_3OH$) except for the different number of Cl^- and solvent molecules, indicating the stability of total **Al_{24}** structure in CH_3OH and CH_2Cl_2 again. Meanwhile, **1b–1f** ($[Al_{24}(OH)_{32}(CH_3O)_{26}(NAP)_{10}Cl_5(H_2O)_x(CH_3OH)_{4-x}H_3]^{2+}$, x = 4, 3, 2, 1, 0), **2a** ($[Al_{24}(OH)_{32}(CH_3O)_{26}(NAP)_{10}Cl_5(H_2O)_1(CH_3CN)_2(CH_3OH)_3H_3]^{2+}$), **2b** ($[Al_{24}(OH)_{32}(CH_3O)_{26}(NAP)_{10}Cl_5(CH_3CN)_2(CH_3OH)_4H_3]^{2+}$) and **3g** ($[Al_{24}(OH)_{32}(CH_3O)_{25}(NAP)_{11}Cl_4(H_2O)_3(CH_3CN)_4(CH_3OH)_3H_2]^{2+}$) also show the ligand exchange between CH_3O^- and NAP^-.

Similarly, the positive-mode ESI-MS obtained by dissolving the crystals of **Al_{12}** in CH_3OH–CH_2Cl_2 was also monitored at m/z = 1000–6000 (Fig. 6a). Three groups of experimental peaks at m/z = 1950–2020 (**1a–1j**, +2), 2100–2160 (**2a–2f**, +2) and 2290–2330 (**3a–3f**, +2) can be clearly assigned by matching the experimental and simulated isotopic distributions (Fig. 6b–d). Two neighbouring peaks of the three groups of experimental data have the same distances with 14.02 corresponding to $[+CH_3O^- - H_2O + H^+]$ and all formulas of fragments are listed in Table S3.† Regrettably, the molecular ion signal was not detected. **1a–1e** assigned to $[Al_{12}(CH_3O)_{17}(NAP)_{17}(H_2O)_8]^{2+}$ (**1a**); $[Al_{12}(CH_3O)_{16}(NAP)_{18}(H_2O)_1]^{2+}$ (**1b**); $[Al_{12}(CH_3O)_{17}(NAP)_{18}H_1]^{2+}$ (**1c**); $[Al_{12}(CH_3O)_{20}(NAP)_{17}(H_2O)_5H_3]^{2+}$ (**1d**); $[Al_{12}(CH_3O)_{21}(NAP)_{17}(H_2O)_4H_4]^{2+}$ (**1e**), and **2c–2f** assigned to $[Al_{12}(CH_3O)_{14}(NAP)_{20}(H_2O)_5]^{2+}$ (**2c**); $[Al_{12}(CH_3O)_{15}(NAP)_{20}(H_2O)_4H_1]^{2+}$ (**2d**); $[Al_{12}(CH_3O)_{16}(NAP)_{20}(H_2O)_3H_2]^{2+}$ (**2e**); $[Al_{12}(CH_3O)_{17}(NAP)_{20}(H_2O)_2H_3]^{2+}$ (**2f**) coincide with the metallic core of **Al_{12}** whereas the numbers of CH_3O^- and NAP^- are different with the molecular formulas, indicating the occurrence of ligand exchange between CH_3O^-, NAP^- and H_2O. **1f–1i** assigned to $[Al_{11}(CH_3O)_{12}(NAP)_{19}(H_2O)_3]^{2+}$, $[Al_{11}(CH_3O)_{13}(NAP)_{19}(H_2O)_2H_1]^{2+}$, $[Al_{11}(CH_3O)_{14}(NAP)_{19}(H_2O)_1H_2]^{2+}$, and $[Al_{11}(CH_3O)_{15}(NAP)_{19}H_3]^{2+}$ lost a metal ion compared with **Al_{12}** and **1j** assigned to $[Al_{10}(CH_3O)_8(NAP)_{20}(H_2O)_5]^{2+}$ has two fewer metal ions than **Al_{12}**. Interestingly, the fragments of **2a–2b** with the corresponding attribution of $[Al_{13}(CH_3O)_{20}(NAP)_{19}(H_2O)_1H_2]^{2+}$ and $[Al_{13}(CH_3O)_{21}(NAP)_{19}H_3]^{2+}$, and **3a–3f** with the corresponding attribution of $[Al_{14}(CH_3O)_{20}(NAP)_{20}(H_2O)_9]^{2+}$, $[Al_{14}(CH_3O)_{21}(NAP)_{20}(H_2O)_8H_1]^{2+}$, $[Al_{14}(CH_3O)_{22}(NAP)_{20}(H_2O)_7H_2]^{2+}$, $[Al_{14}(CH_3O)_{23}(NAP)_{20}(H_2O)_6H_3]^{2+}$, $[Al_{14}(CH_3O)_{24}(NAP)_{20}(H_2O)_5H_4]^{2+}$, $[Al_{14}(CH_3O)_{25}$

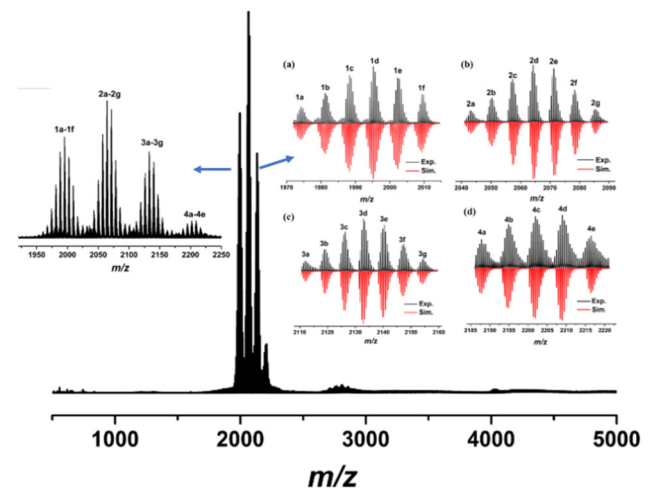

Fig. 5 The positive-ion ESI-MS of **Al_{24}** in CH_3OH/CH_2Cl_2. Left inset: the experimental isotropic pattern. Right inset: the experimental isotropic pattern (block) and simulated (red) data.

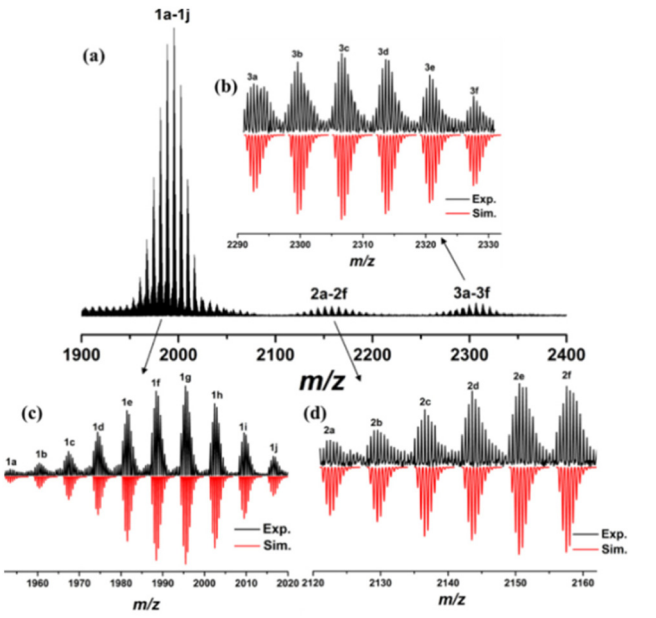

Fig. 6 (a) The positive-ion ESI-MS of **Al_{12}** in CH_3OH/CH_2Cl_2. The experimental isotropic pattern (block) and simulated (red) data for 1 group (c), 2 group (d), and 3 group (b).

This journal is © the Partner Organisations 2023

Published on 28 1 2023. Downloaded on 2025/10/16 18:37:51.

$(NAP)_{20}(H_2O)_4H_5]^{2+}$ display the increase of a and two Al^{3+} ions for **Al_{12}**. The above analysis result indicates that the metal skeleton of the **Al_{12}** cluster can be partly stable in CH_3OH and CH_2Cl_2, while some fragments with adjacent nuclear numbers, *e.g.*, Al_{10}, Al_{11}, Al_{13}, Al_{14} exist in CH_3OH and CH_2Cl_2. Alternatively, the number of CH_3O^- is less than the theoretical 24, whereas that of NAP^- is more. Thus, we surmise that NAP^- firstly coordinated with Al^{3+} ions in the assembly process of **Al_{12}**, and was later replaced by CH_3O^-. Besides, the negative-ion ESI-MS data of **Al_{12}** obtained by dissolving its crystals in CH_3OH–CH_2Cl_2 was monitored at m/z = 500–6000 (Fig. S2†). Only a small fragment peak at m/z = 863.15 was detected at m/z = 500–6000 and there are no more pieces of information.

UV–Vis spectra and photocurrent measurements of Al_{24} and Al_{12}

The solid-state ultraviolet-visible absorption spectra (UV-Vis) of HNAP, **Al_{24}**, and **Al_{12}** were recorded at room temperature. As shown in Fig. S3a and S3b,† the HNAP ligand exhibits absorption at 210 nm, whereas **Al_{24}** and **Al_{12}** have a similar broad absorption band at 250–400 nm. The red-shifted phenomenon may be caused by Al-perturbed $\pi \rightarrow \pi^*$ transition of the ligand.[61] The band gaps (E_g) of **Al_{24}** and **Al_{12}** are 3.48 and 3.44 eV calculated based on the Kubelka–Munk function, respectively (Fig. S4†),[62] which are much smaller than 9 eV of Al_2O_3.[63] This reveals that the aggregation of aluminum ions into aluminum-oxo clusters affects the band gap structure, including the widening of the absorption edge and the narrowing of the band gap.

The photocurrent responses of **Al_{24}** and **Al_{12}** under LED light were further examined by the typical three-electrode system. The working electrode was indium tin oxide (ITO) glass, the auxiliary electrode was platinum wire, and the reference electrode was Ag/AgCl, maintaining the bias voltage of 0.6 V in the meantime. As shown in Fig. 7, upon on–off cycling exposure with LED light (λ = 365 nm and 420 nm; 10 s intervals; 50 W), obvious photocurrent reactions were observed, and the photocurrent densities exhibit a promptly rising or fast falling under light irradiation or no irradiation conditions. This indicates that **Al_{12}** and **Al_{24}** both have fast response speeds to LED light. No matter whether the irradiations wavelengths are at 420 nm or 365 nm, **Al_{12}** generates higher photocurrent values than these of **Al_{24}**, which demonstrates that more efficient generation and separation of photoinduced electron/hole pairs were observed in ITO electrodes of **Al_{12}** under the LED light. This could be explained on the basis of the lower band gap of **Al_{12}** at 3.44 eV.[64] The above experimental results exhibiting **Al_{12}** and **Al_{24}** are a kind of potential photoelectric materials.

Luminescence properties of Al_{24} and Al_{12}

At room temperature, the solid-state luminescence properties of HNAP, **Al_{24}**, and **Al_{12}** were observed (Fig. S5†). The maximum emission of HNAP was at 372 nm under a maximum excitation wavelength of 319 nm (Fig. S5a and 5b†), which originated from the intramolecular π–π^* transition of the HNAP organic ligand. As illustrated in Fig. S5c and 5d,† the **Al_{24}** cluster exhibits the ligand-centered blue fluorescence

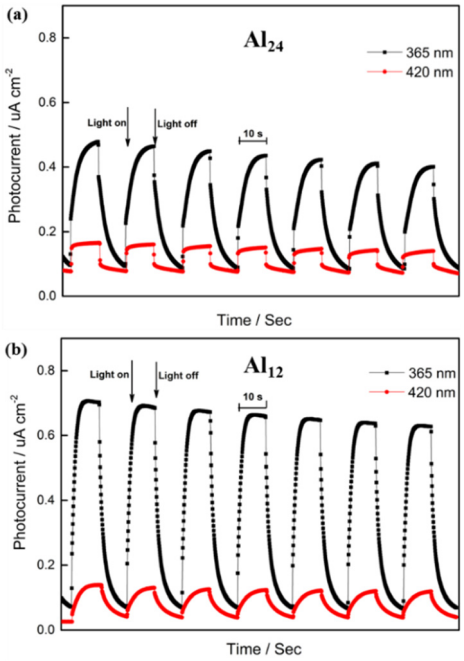

Fig. 7 Transient photocurrent responses of **Al_{24}** (a) and **Al_{12}** (b).

with emission at 374 nm under 319 nm excitation. A similar blue fluorescence from ligand-centered emission is also observed in **Al_{12}** with the maximum emission wavelength at 389 nm under 352 nm excitation (Fig. S5e and 5f†).

To determine their potential applications as optical thermometers, the operating range for the temperature-dependent luminescence spectra of **Al_{24}** and **Al_{12}** was from 300 to 120 K. The temperature was changed from 300 K to 120 K, but the emission location of the **Al_{24}** cluster remained fixed at x = 0.15 and y = 0.06 in the CIE space (Fig. S6a and Table S5†) in the blue-light region (Fig. 8a). Furthermore, the emission position

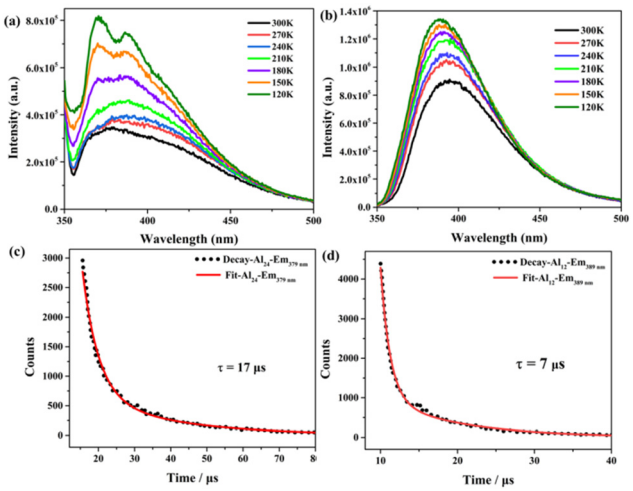

Fig. 8 The temperature-dependent luminescence spectra of **Al_{24}** (a) and **Al_{12}** (b) from 300 K to 120 K. Luminescence lifetimes of **Al_{24}** (c, λ_{em} = 379 nm) and **Al_{12}** (d, λ_{em} = 389 nm) at room temperature.

Published on 28 1 2023. Downloaded on 2025/10/16 18:37:51.

of $\mathbf{Al_{12}}$ is slightly blue-shifted from 394.5 nm to 387.5 nm, as the temperature drops from 300 K to 120 K (Fig. 8b) while the CIE coordinates of the emission positions change from x = 0.16, y = 0.05 to x = 0.17, y = 0.07 (Fig. S6b and Table S5†). The probable reason is the restricted rotation of ligands in $\mathbf{Al_{12}}$ at lower temperatures. In addition, the emission intensity of $\mathbf{Al_{24}}$ and $\mathbf{Al_{12}}$ gradually increased with decreasing temperature on account of the reduction of non-radiative decay.

The time-resolved decay curves of the $\mathbf{Al_{24}}$ and $\mathbf{Al_{12}}$ clusters were recorded at room temperature, and their fitting results show the double exponential functions. The lifetimes of $\mathbf{Al_{24}}$ and $\mathbf{Al_{12}}$ are 17 μs (λ_{em} = 379 nm; τ_1 = 4.44, 37%; τ_2 = 24.4, 63%; Fig. 8c) and 7 μs (λ_{em} = 389 nm; τ_1 = 1.26, 35%; τ_2 = 10.26, 65%; Fig. 8d). The absolute solid-state quantum yields of the $\mathbf{Al_{24}}$ and $\mathbf{Al_{12}}$ are 25.11% and 18.42%, respectively. The different luminescence behaviours of $\mathbf{Al_{24}}$ and $\mathbf{Al_{12}}$ can be attributed to the different ligand environments in the crystalline structures, generating the different constraints on the rotation of the NAP^- ligands.

Conclusions

In summary, we synthesized an $\mathbf{Al_{12}}$ molecular ring and a rare $\mathbf{Al_{24}}$ metallocage based on the NAP^- ligand obtained by modulating the solvent in a simple one-pot solvothermal reaction. The $\mathbf{Al_{12}}$ is a dodecagonal molecular ring and the $\mathbf{Al_{24}}$ metallocage can be seen as a truncated cube composed of eight Al_3 triangles and six Al_8 octagons formed by sharing vertical Al^{3+} ions, realizing the complete change of Al-oxo skeletons. Interestingly, the $\mathbf{Al_{12}}$ and $\mathbf{Al_{24}}$ clusters exhibited the photocurrent-generating capacity and luminescent behaviour, indicating that the Al clusters are potentially photocatalytic and luminescent materials.

Conflicts of interest

There are no conflicts to declare.

Acknowledgements

This work was supported by the National Natural Science Foundation of China (no. 22101148) and the Natural Science Foundation of Shandong Province (no. ZR2021QB008).

References

1 S. Schein and J. M. Gayed, Fourth class of convex equilateral polyhedron with polyhedral symmetry related to fullerenes and viruses, *Proc. Natl. Acad. Sci. U. S. A.*, 2014, **111**, 2920–2925.
2 C. Stump, AI aids intuition in mathematical discovery, *Nature*, 2021, **600**, 44–45.
3 I. Severcan, C. Geary, A. Chworos, N. Voss, E. Jacovetty and L. Jaeger, A polyhedron made of tRNAs, *Nat. Chem.*, 2010, **2**, 772–779.
4 R. Twarock and A. Luque, Structural puzzles in virology solved with an overarching icosahedral design principle, *Nat. Commun.*, 2019, **10**, 4414.
5 R. Iinuma, Y. Ke, R. Jungmann, T. Schlichthaerle, J. B. Woehrstein and P. Yin, Polyhedra Self-Assembled from DNA Tripods and Characterized with 3D DNA-PAINT, *Science*, 2014, **344**, 65–69.
6 J.-P. Lang, Q.-F. Xu, Z.-N. Chen and B. F. Abrahams, Assembly of a Supramolecular Cube, $[(Cp^*WS_3Cu_3)_8Cl_8(CN)_{12}Li_4]$ from a Preformed Incomplete Cubane-like Compound $[PPh_4][Cp^*WS_3(CuCN)_3]$, *J. Am. Chem. Soc.*, 2003, **125**, 12682–12683.
7 S. R. Seidel and P. J. Stang, High-Symmetry Coordination Cages via Self-Assembly, *Acc. Chem. Res.*, 2002, **35**, 972–983.
8 A. V. Virovets, E. Peresypkina and M. Scheer, Structural Chemistry of Giant Metal Based Supramolecules, *Chem. Rev.*, 2021, **121**, 14485–14554.
9 D. Fujita, Y. Ueda, S. Sato, N. Mizuno, T. Kumasaka and M. Fujita, Self-assembly of tetravalent Goldberg polyhedra from 144 small components, *Nature*, 2016, **540**, 563–566.
10 X. Z. Li, C. B. Tian and Q. F. Sun, Coordination-Directed Self-Assembly of Functional Polynuclear Lanthanide Supramolecular Architectures, *Chem. Rev.*, 2022, **122**, 6374–6458.
11 S. J. Bao, Z. M. Xu, T. C. Yu, Y. L. Song, H. Wang, Z. Niu, X. Li, B. F. Abrahams, P. Braunstein and J. P. Lang, Flexible Vertex Engineers the Controlled Assembly of Distorted Supramolecular Tetrahedral and Octahedral Cages, *Research*, 2022, **2022**, 9819343.
12 S. J. Bao, Z. M. Xu, Y. Ju, Y. L. Song, H. Wang, Z. Niu, X. Li, P. Braunstein and J. P. Lang, The Covalent and Coordination Co-Driven Assembly of Supramolecular Octahedral Cages with Controllable Degree of Distortion, *J. Am. Chem. Soc.*, 2020, **142**, 13356–13361.
13 Z. H. Wei, C. Y. Ni, H. X. Li, Z. G. Ren, Z. R. Sun and J. P. Lang, $[PyH][\{TpMo(\mu_3\text{-}S)_4Cu_3\}_4(\mu_{12}\text{-}I)]$: a unique tetracubane cluster derived from the S-S bond cleavage and the iodide template effects and its enhanced NLO performances, *Chem. Commun.*, 2013, **49**, 4836–4838.
14 L. Yang, X.-Y. Wang, X.-Y. Tang, M.-Y. Wang, C.-Y. Ni, H. Yu, Y.-L. Song, B. F. Abrahams and J.-P. Lang, Temperature-dependent chloride-mediated access to atom-precise silver thiolate nanoclusters, *Sci. China: Chem.*, 2022, **65**, 1094–1099.
15 H. W. Kroto, J. R. Heath, S. C. O'Brien, R. F. Curl and R. E. Smalley, C_{60}: Buckminsterfullerene, *Nature*, 1985, **318**, 162–163.
16 J. Spandl, I. Brüdgam and H. Hartl, Solvothermal Synthesis of a 24-Nuclear, Cube-Shaped Squarato-oxovanadium(IV) Framework: $[N(nBu)_4]_8[V_{24}O_{24}(C_4O_4)_{12}(OCH_3)_{32}]$, *Angew. Chem., Int. Ed.*, 2001, **40**, 4018–4020.

 This journal is © the Partner Organisations 2023

Published on 28 1 2023. Downloaded on 2025/10/16 18:37:51.

17 Y. Bi, S. Du and W. Liao, Thiacalixarene-based nanoscale polyhedral coordination cages, *Coord. Chem. Rev.*, 2014, **276**, 61–72.
18 S. P. Argent, A. Greenaway, M. d. C. Gimenez-Lopez, W. Lewis, H. Nowell, A. N. Khlobystov, A. J. Blake, N. R. Champness and M. Schroder, High-nuclearity metal-organic nanospheres: a Cd_{66} ball, *J. Am. Chem. Soc.*, 2012, **134**, 55–58.
19 J. Lin, N. Li, S. Yang, M. Jia, J. Liu, X. M. Li, L. An, Q. Tian, L. Z. Dong and Y. Q. Lan, Self-Assembly of Giant Mo_{240} Hollow Opening Dodecahedra, *J. Am. Chem. Soc.*, 2020, **142**, 13982–13988.
20 N. T. Tran, D. R. Powell and L. F. Dahl, Nanosized $Pd_{145}(CO)_x(PEt_3)_{30}$ Containing a Capped Three-Shell 145-Atom Metal-Core Geometry of Pseudo Icosahedral Symmetry, *Angew. Chem., Int. Ed.*, 2000, **39**, 4121–4125.
21 Z. Wang, H. F. Su, Y. Z. Tan, S. Schein, S. C. Lin, W. Liu, S. A. Wang, W. G. Wang, C. H. Tung, D. Sun and L. S. Zheng, Assembly of silver Trigons into a buckyball-like Ag_{180} nanocage, *Proc. Natl. Acad. Sci. U. S. A.*, 2017, **114**, 12132–12137.
22 J. B. Peng, X. J. Kong, Q. C. Zhang, M. Orendac, J. Prokleska, Y. P. Ren, L. S. Long, Z. Zheng and L. S. Zheng, Beauty, symmetry, and magnetocaloric effect-four-shell keplerates with 104 lanthanide atoms, *J. Am. Chem. Soc.*, 2014, **136**, 17938–17941.
23 S. L. Heath, P. A. Jordan, I. D. Johnson, G. R. Moore, A. K. Powell and M. Helliwell, Comparative X-ray and ^{27}Al NMR spectroscopic studies of the speciation of aluminum in aqueous systems: Al(III) complexes of $N(CH_2CO_2H)_2(CH_2CH_2OH)$, *J. Inorg. Biochem.*, 1995, **59**, 785–794.
24 S. Abeysinghe, D. K. Unruh and T. Z. Forbes, Crystallization of Keggin-Type Polyaluminum Species by Supramolecular Interactions with Disulfonate Anions, *Cryst. Growth Des.*, 2012, **12**, 2044–2051.
25 W. Wang, K. M. Wentz, S. E. Hayes, D. W. Johnson and D. A. Keszler, Synthesis of the hydroxide cluster $[Al_{13}(\mu_3\text{-}OH)_6(\mu\text{-}OH)_{18}(H_2O)_{24}]^{15+}$ from an aqueous solution, *Inorg. Chem.*, 2011, **50**, 4683–4685.
26 B. L. Fulton, C. K. Perkins, R. H. Mansergh, M. A. Jenkins, V. Gouliouk, M. N. Jackson, J. C. Ramos, N. M. Rogovoy, M. T. Gutierrez-Higgins, S. W. Boettcher, J. F. Conley, D. A. Keszler, J. E. Hutchison and D. W. Johnson, Minerals to Materials: Bulk Synthesis of Aqueous Aluminum Clusters and Their Use as Precursors for Metal Oxide Thin Films, *Chem. Mater.*, 2017, **29**, 7760–7765.
27 S. E. Smart, J. Vaughn, I. Pappas and L. Pan, Controlled step-wise isomerization of the Keggin-type Al_{13} and determination of the γ-Al_{13} structure, *Chem. Commun.*, 2013, **49**, 11352–11354.
28 L. Allouche, C. Gérardin, T. Loiseau, G. Férey and F. Taulelle, Al_{30}: A Giant Aluminum Polycation, *Angew. Chem., Int. Ed.*, 2000, **39**, 511–514.
29 K. S. Lokare, N. Frank, B. Braun-Cula, I. Goikoetxea, J. Sauer and C. Limberg, Trapping Aluminum Hydroxide Clusters with Trisilanols during Speciation in Aluminum (III)-Water Systems: Reproducible, Large Scale Access to Molecular Aluminate Models, *Angew. Chem., Int. Ed.*, 2016, **55**, 12325–12329.
30 W. Schmitt, E. Baissa, A. Mandel, C. E. Anson and A. K. Powell, $[Al_{15}(\mu_3\text{-}O)_4(\mu_3\text{-}OH)_6(\mu\text{-}OH)_{14}(hpdta)_4]^{3-}$—A New Al_{15} Aggregate Which Forms a Supramolecular Zeotype, *Angew. Chem., Int. Ed.*, 2001, **40**, 3577–3581.
31 E. A. Cochran, K. N. Woods, D. W. Johnson, C. J. Page and S. W. Boettcher, Unique chemistries of metal-nitrate precursors to form metal-oxide thin films from solution: materials for electronic and energy applications, *J. Mater. Chem. A*, 2019, **7**, 24124–24149.
32 Y. J. Liu, Q. H. Li, D. J. Li, X. Z. Zhang, W. H. Fang and J. Zhang, Designable Al_{32}-Oxo Clusters with Hydrotalcite-like Structures: Snapshots of Boundary Hydrolysis and Optical Limiting, *Angew. Chem., Int. Ed.*, 2021, **60**, 4849–4854.
33 Y. Li, C. Zheng, S. T. Wang, Y. J. Liu, W. H. Fang and J. Zhang, Record Aluminum Molecular Rings for Optical Limiting and Nonlinear Optics, *Angew. Chem., Int. Ed.*, 2022, **61**, e202116563.
34 S. T. Wang, Y. J. Liu, C. C. Feng, W. H. Fang and J. Zhang, The largest aluminum molecular rings: Phenol-thermal synthesis, photoluminescence, and optical limiting, *Aggregate*, 2022, e264.
35 Y. J. Liu, Y. F. Sun, S. H. Shen, S. T. Wang, Z. H. Liu, W. H. Fang, D. S. Wright and J. Zhang, Water-stable porous Al24 Archimedean solids for removal of trace iodine, *Nat. Commun.*, 2022, **13**, 6632.
36 L. Geng, C. H. Liu, S. T. Wang, W. H. Fang and J. Zhang, Designable Aluminum Molecular Rings: Ring Expansion and Ligand Functionalization, *Angew. Chem., Int. Ed.*, 2020, **59**, 16735–16740.
37 X. Z. Zhang, X. F. Wang, W. H. Fang and J. Zhang, Synthesis, Structures, and Fluorescence Properties of Dimeric Aluminum Oxo Clusters, *Inorg. Chem.*, 2021, **60**, 7089–7093.
38 O. V. B. Dolomanov, L. J. Bourhis, R. J. Gildea, J. A. K. Howard and H. Puschmann, OLEX2: a complete structure solution, refinement and analysis program, *J. Appl. Crystallogr.*, 2009, **42**, 339–341.
39 G. M. Sheldrick, A short history of SHELX, *Acta Crystallogr., Sect. A: Found. Crystallogr.*, 2008, **64**, 112–122.
40 A. L. Spek, Structure validation in chemical crystallography, *Acta Crystallogr., Sect. D: Biol. Crystallogr.*, 2009, **65**, 148.
41 X. Y. Li, H. F. Su, Q. W. Li, R. Feng, H. Y. Bai, H. Y. Chen, J. Xu and X. H. Bu, A Giant Dy_{76} Cluster: A Fused Bi-Nanopillar Structural Model for Lanthanide Clusters, *Angew. Chem., Int. Ed.*, 2019, **58**, 10184–10188.
42 M. Wu, F. Jiang, D. Yuan, J. Pang, J. Qian, S. A. Al-Thabaiti and M. Hong, Polymeric double-anion templated Er_{48} nanotubes, *Chem. Commun.*, 2014, **50**, 1113–1115.
43 F.-S. Guo, Y.-C. Chen, L.-L. Mao, W.-Q. Lin, J.-D. Leng, R. Tarasenko, M. Orendáč, J. Prokleška, V. Sechovský and M.-L. Tong, Anion-Templated Assembly and

Published on 28 1 2023. Downloaded on 2025/10/16 18:37:51.

Magnetocaloric Properties of a Nanoscale {Gd_{38}} Cage versus a {Gd_{48}} Barrel, *Chem. – Eur. J.*, 2013, **19**, 14876–14885.

44 X.-Y. Li, Y. Jing, J. Zheng, H. Ding, Q. Li, M.-H. Yu and X.-H. Bu, Two Luminescent High-Nuclearity Lanthanide Clusters Ln_{48} (Ln = Eu and Tb) with a Nanopillar Structure, *Cryst. Growth Des.*, 2020, **20**, 5294–5301.

45 R. Wang, Z. Zheng, T. Jin and R. J. Staples, Coordination Chemistry of Lanthanides at "High" pH: Synthesis and Structure of the Pentadecanuclear Complex of Europium (III) with Tyrosine, *Angew. Chem.*, 1999, **111**, 1929–1932.

46 W. Huang, Z. Zhang, Y. Wu, W. Chen, D. A. Rotsch, L. Messerle and Z. Zheng, A systematic study of halide-template effects in the assembly of lanthanide hydroxide cluster complexes with histidine, *Inorg. Chem. Front.*, 2021, **8**, 26–34.

47 D. T. Thielemann, A. T. Wagner, Y. Lan, P. Ona-Burgos, I. Fernandez, E. S. Rosch, D. K. Kolmel, A. K. Powell, S. Brase and P. W. Roesky, Peptoid-ligated pentadecanuclear yttrium and dysprosium hydroxy clusters, *Chem. – Eur. J.*, 2015, **21**, 2813–2820.

48 X. Y. Li, H. F. Su, K. Yu, Y. Z. Tan, X. P. Wang, Y. Q. Zhao, D. Sun and L. S. Zheng, A platonic solid templating Archimedean solid: an unprecedented nanometre-sized Ag_{37} cluster, *Nanoscale*, 2015, **7**, 8284–8288.

49 Y. Bi, X.-T. Wang, W. Liao, X. Wang, X. Wang, H. Zhang and S. Gao, A {Co_{32}} Nanosphere Supported by p-tert-Butylthiacalix[4]arene, *J. Am. Chem. Soc.*, 2009, **131**, 11650–11651.

50 X.-J. Kong, Y. Wu, L.-S. Long, L.-S. Zheng and Z. Zheng, A Chiral 60-Metal Sodalite Cage Featuring 24 Vertex-Sharing [$Er_4(\mu_3\text{-}OH)_4$] Cubanes, *J. Am. Chem. Soc.*, 2009, **131**, 6918–6919.

51 Y. Domoto, M. Abe and M. Fujita, A Highly Entangled $(M_3L_2)_8$ Truncated Cube from the Anion-Controlled Oligomerization of a pi-Coordinated M_3L_2 Subunit, *J. Am. Chem. Soc.*, 2021, **143**, 8578–8582.

52 K. Su, M. Wu, D. Yuan and M. Hong, Interconvertible vanadium-seamed hexameric pyrogallol[4]arene nanocapsules, *Nat. Commun.*, 2018, **9**, 4941.

53 L. Tang, A. Ma, C. Zhang, X. Liu, R. Jin and S. Wang, Total Structure of Bimetallic Core-Shell $[Au_{42}Cd_{40}(SR)_{52}]^{2-}$ Nanocluster and Its Implications, *Angew. Chem., Int. Ed.*, 2021, **60**, 17969–17973.

54 S. Lee, M. S. Bootharaju, G. Deng, S. Malola, W. Baek, H. Hakkinen, N. Zheng and T. Hyeon, $[Cu_{32}(PET)_{24}H_8Cl_2](PPh_4)_2$: A Copper Hydride Nanocluster with a Bisquare Antiprismatic Core, *J. Am. Chem. Soc.*, 2020, **142**, 13974–13981.

55 J. J. Li, Z. J. Guan, Z. Lei, F. Hu and Q. M. Wang, Same Magic Number but Different Arrangement: Alkynyl-Protected Au_{25} with D_3 Symmetry, *Angew. Chem., Int. Ed.*, 2019, **58**, 1083–1087.

56 Y.-K. Deng, H.-F. Su, J.-H. Xu, W.-G. Wang, M. Kurmoo, S.-C. Lin, Y.-Z. Tan, J. Jia, D. Sun and L.-S. Zheng, Hierarchical Assembly of a $\{Mn^{II}_{15}Mn^{III}_{4}\}$ Brucite Disc: Step-by-Step Formation and Ferrimagnetism, *J. Am. Chem. Soc.*, 2016, **138**, 1328–1334.

57 X. Y. Li, H. F. Su, M. Kurmoo, C. H. Tung, D. Sun and L. S. Zheng, Structure, solution assembly, and electroconductivity of nanosized argento-organic-cluster/framework templated by chromate, *Nanoscale*, 2017, **9**, 5305–5314.

58 X. Y. Li, H. F. Su, Q. W. Li, R. Feng, H. Y. Bai, H. Y. Chen, J. Xu and X. H. Bu, A Giant Dy_{76} Cluster: A Fused Bi-Nanopillar Structural Model for Lanthanide Clusters, *Angew. Chem., Int. Ed.*, 2019, **58**, 10184–10188.

59 H. Zheng, M.-H. Du, S.-C. Lin, Z.-C. Tang, X.-J. Kong, L.-S. Long and L.-S. Zheng, Assembly of a Wheel-Like $Eu_{24}Ti_8$ Cluster under the Guidance of High-Resolution Electrospray Ionization Mass Spectrometry, *Angew. Chem., Int. Ed.*, 2018, **57**, 10976–10979.

60 Y.-Y. Zhang, D.-S. Zhang, T. Li, M. Kurmoo and M.-H. Zeng, In Situ Metal-Assisted Ligand Modification Induces Mn_4 Cluster-to-Cluster Transformation: A Crystallography, Mass Spectrometry, and DFT Study, *Chem. – Eur. J.*, 2020, **26**, 721–728.

61 J. H. Weber, Complexes of pyrrole-derivative ligands. I., Planar nickel(II) complexes with tetradentate ligands, *Inorg. Chem.*, 1967, **6**, 258–262.

62 Y. Mu, D. Wang, X.-D. Meng, J. Pan, S.-D. Han and Z.-Z. Xue, Construction of Iodoargentates with Diverse Architectures: Template Syntheses, Structures, and Photocatalytic Properties, *Cryst. Growth Des.*, 2020, **20**, 1130–1138.

63 K. Matsunaga, T. Mizoguchi, A. Nakamura, T. Yamamoto and Y. Ikuhara, Formation of titanium-solute clusters in alumina: A first-principles study, *Appl. Phys. Lett.*, 2004, **84**, 4795–4797.

64 A. Kongkanand, K. Tvrdy, K. Takechi, M. Kuno and P. V. Kamat, Quantum Dot Solar Cells. Tuning Photoresponse through Size and Shape Control of CdSe–TiO_2 Architecture, *J. Am. Chem. Soc.*, 2008, **130**, 4007–4015.

 This journal is © the Partner Organisations 2023